Nanoscale

PAPER

View Article Online
View Journal | View Issue

Cite this: *Nanoscale*, 2014, **6**, 207

Facile and novel electrochemical preparation of a graphene–transition metal oxide nanocomposite for ultrasensitive electrochemical sensing of acetaminophen and phenacetin†

Lin Jiang, Shuqing Gu, Yaping Ding,* Feng Jiang and Zhen Zhang

Received 15th July 2013
Accepted 1st October 2013

DOI: 10.1039/c3nr03620k

www.rsc.org/nanoscale

A facile and novel preparation strategy based on electrochemical techniques for the fabrication of electrodeposited graphene (EGR) and zinc oxide (ZnO) nanocomposite was developed. The morphology and structure of the EGR-based nanocomposite were investigated by scanning electron microscopy (SEM), transmission electron microscopy (TEM), energy dispersive X-ray spectroscopy (XPS) and Raman spectroscopy. Meanwhile, the electrochemical performance of the nanocomposite was demonstrated with cyclic voltammetry (CV) and electrochemical impedance spectroscopy (EIS). Due to the synergistic effect of EGR and ZnO nanoparticles, an ultrasensitive electrochemical sensor for acetaminophen (AC) and phenacetin (PCT) was successfully fabricated. The linearity ranged from 0.02 to 10 μM for AC and 0.06 to 10 μM for PCT with high sensitivities of 54 295.82 μA mM^{-1} cm^2 for AC and 21 344.66 μA mM^{-1} cm^2 for PCT, respectively. Moreover, the practical applicability was validated to be reliable and desirable in pharmaceutical detections. The excellent results showed the promise of the proposed preparation strategy of EGR–transition metal oxide nanocomposite in the field of electroanalytical chemistry.

1. Introduction

The last decade has witnessed a spectacular evolution of graphene (GR)–transition metal hybrid nanomaterials in electrochemical fields owing to the exceptional electrochemical and structural properties of GR as well as the catalytic characteristics of transition metals.[1–9] These multifunctional hybrids have been demonstrated to be significantly promising by various outstanding fruits in fields like Li-ion batteries and storage, supercapacitors and electrochemical sensors. For instance, Zhou *et al.*[1] synthesized a durable high-rate CuO hollow nanoparticle–GR-nanosheet composite as an anode material for lithium-ion batteries. Li *et al.*[6] studied NiAl-layered double hydroxide–GR hybrids for dopamine detection. Chen *et al.*[7] proposed GR–copper nanoparticle composites for electrochemical sensing of carbohydrates. Our groups have also reported sensitive electrochemical sensors for L-tryptophan and L-tyrosine utilizing Co_3O_4 together with GR as enhanced materials.[10,11] All these works effectively drive the electrochemistry realm to a new era.

Nonetheless, challenges still pervasively exist. Chemically reduced GR generally suffers from contamination by excessive reducing agents to the products, which brings about unsatisfactory results in application.[12] Meanwhile, strong van der Waals interactions (5.9 kJ mol^{-1} carbon)[13] between GR sheets tends to result in the re-stacking of GR. Together with oxidation effects, these problems give rise to the loss and even deprivation of diffusion rates and outstanding specific surface of GR, and further limit its application in various fields.[14,15] With regard to transition metals, the typical fabrication procedures tend to be time-consuming and toxic. Moreover, trivial processing and high temperature operations indispensably require certain manual labor, equipment and valuable time. Sintering and dissolution problems, unfortunately, always tangle the cyclic performance and working life of metal-based materials during application. Additionally, GR–metal composite synthesis processes inevitably result in a certain degree of waste and some irreversible changes of the GR sheets, further leading to the failure of the expectantly effective synergy of GR and metals. Thus, a facile and novel preparation strategy for GR–metal composites is of considerable significance for both effective and efficient applications.

Recently, electrochemical techniques have emerged as effective tools for rapid, facile and effective synthesis of various materials. The main principle is based on the impetus of the electrochemical power to change the Fermi energy level of the electrode materials surface.[16] Up to now, cyclic voltammetry,[17–20] electrochemical potential pulse techniques,[21,22] galvanostatic methods[23,24] and potentiostatic deposition[25,26] have been

Department of Chemistry, Shanghai University, Shanghai 200444, P. R. China. E-mail: wdingyp@sina.com; Fax: +86 21 66132797; Tel: +86 21 66134734

† Electronic supplementary information (ESI) available. See DOI: 10.1039/c3nr03620k

applied to material preparations. Among them, potentiostatic methods not only ensure similar film thicknesses, but also minimize the risk of unwanted side reactions that can occur during polymerization.[25] Actually, multi-walled carbon nanotubes (MWCNTs) have been successfully fabricated *via* potentiostatic methods for electrochemical sensing.[27,28] Yet, until now, there have been no reports concerning electrochemical sensors based on potentiostatically manufactured GR hybrids. Thus, there is a substantially promising development space in this booming field.

Aiming to explore the unrevealed sensing potential of electrodeposited GR (EGR) and conquer the existing challenges, a facile and novel method has been employed to prepare EGR–zinc oxide (EGR–ZnO) *via* a cooperation of the potentiostatic technique and cyclic voltammetry (CV) for electrochemical sensing. The novel EGR film, accompanied by ZnO nanoparticles, is expected to be more biocompatible and sensitive for electroanalysis. Meanwhile, acetaminophen (AC) and phenacetin (PCT) were selected to explore the practical performance of the proposed material. AC and PCT both play important antipyretic and antalgic roles in daily life. While AC is more common and manifests fewer side effects, PCT merely exists in compound drugs currently since it has a severe negative impact on human tissues and organs. However, there is a considerable probability of coinstantaneous intake of AC and PCT in daily life, causing an unnecessarily repetitive ingestion of analgesics. Worse still, the damages are extremely threatening to humans, including liver, kidney and even human life. Therefore, the establishment of a sensitive and simultaneous determination for AC and PCT is not only essential for human health and security, but also an innovative behavior in analytical fields. As expected, the work presented here indicated the effectiveness and feasibility of the proposed strategy and the great potential of EGR–transition metal composites in electroanalytical fields.

2. Experimental

2.1 Reagents and apparatus

Graphene was purchased from XFNANO, INC (Nanjing, China). AC, PCT, theophylline, glycine, alanine, phenylalanine and leucine were purchased from Aladdin Chemical Reagent Co., Ltd. (Shanghai, China). Glucose, maltose, sucrose and other chemicals were obtained from Sinopharm Chemical Reagent Co., Ltd. (SCRC, China). All chemicals employed in this work were analytical grade. All experiments were performed in 0.1 M phosphate buffer solution (PBS) and double distilled water was used throughout. The drug samples of AC and PCT were purchased from a local pharmacy. All electrochemical experiments were carried out at room temperature.

Electrochemical experiments including CV and square wave voltammetry (SWV) were all carried out with a CHI 842B electrochemical workstation (Chenhua Corp. Shanghai, China). Electrochemical impedance spectroscopy (EIS) was performed on a CHI 660D electrochemical workstation (Chenhua Corp. Shanghai, China). A conventional three-electrode system was employed throughout the experiments with a glassy carbon electrode (GCE) (3 mm in diameter) as the working electrode, a platinum electrode as the counter electrode, and a saturated calomel electrode as the reference electrode. The pH value was determined with a pHS-3C acidity meter. Scanning electron micrographs (SEM) were carried out using a scanning electron microscope (JSM-6700F, 15.0 kV). High resolution transmission electron microscopy (HRTEM) was obtained on a JEM-2010F (Japan). X-ray photoelectron spectroscopy (XPS) analysis was carried out on a RBD upgraded PHI-5000C ESCA system (Perkin Elmer) with Mg Kα radiation ($h\nu = 1253.6$ eV) or Al Kα radiation ($h\nu = 1486.6$ eV). Raman scattering was performed on an INVIA (England) Raman Microscope using a 545.5 nm laser source.

2.2 Preparation of modified electrodes

Before modification, a bare GCE of 3 mm diameter was firstly polished on a chamois leather with alumina slurries until a mirror-like surface was acquired. Then the GCE was ultrasonicated in HNO_3 solution (1 : 1), ethanol and double distilled water for 5 min each. The EGR/GCE was gained *via* electrodeposition by applying a potentiostatic potential of +1.8 V in 0.1 M KCl containing 200 μL 1 mg mL^{-1} GR. A dropped-graphene (DGR) modified GCE (DGR/GCE) was also prepared for the aim of comparison. It was obtained by dropping 6 μL pristine GR–Nafion (1 mg mL^{-1}) on the GCE and dried under an infrared lamp. Then, the EGR/GCE or GCE was respectively immersed into 0.02 M $Zn(NO_3)_2$ in 0.1 M KCl aqueous solution and subject to 25 scans of CV in the potential range of −0.8 to 1.5 V at 100 mV s^{-1} to electrodeposit ZnO nanoparticles on the electrode surface to obtain the ZnO/EGR/GCE and ZnO/GCE respectively. Eventually, the as-prepared electrodes were rinsed carefully with double distilled water for further use.

2.3 Determination of AC and PCT in formulation tablets

The developed sensor was employed for drug tablet determination. Compound paracetamol–amantadine hydrochloride capsules were chosen as the AC drug sample. Somedon, a common compound drug for alleviating pain and ache, was selected as the sample for PCT. Five tablets of AC and PCT were selected at random, and thoroughly ground. An accurately weighed portion of the powder, an amount equivalent to one tablet, was dissolved and transferred into a 100 mL volumetric flask. The solution was shaken and filtrated to make the stock solution, and then diluted to a series of concentrations for determination. The samples were stored at 4 °C.

Blood samples obtained from a healthy person were supplied by Shanghai university hospital. A mixture of 1 mL blood sample and 0.15 mL perchloric acid was centrifuged at 2500 rpm for 15 min with the aim of removing redundant protein. After that, the supernatant was directly injected to pH 6.0 PBS to give a total volume of 10 mL for the drug determination in human serum.

3. Results and discussion

3.1 Characterization of EGR–ZnO nanocomposite

3.1.1 TEM and SEM images. The EGR–ZnO nanocomposite film was successfully electrodeposited on GCE from GR and

$Zn(NO_3)_2$ aqueous solutions. The morphology of the modified electrodes was investigated by SEM and TEM. Fig. 1(A–D) illustrates the SEM images and TEM images of the DGR, EGR and ZnO–EGR nanocomposites. As shown in Fig. 1A and B, DGR exhibited a sheet-like appearance with typical transparent and corrugated morphology, indicating the innate large surface area. In stark contrast with DGR, EGR exhibited a finer crimpled structure compared to DGR under the same magnification of SEM. It was anticipated that the EGR film with a distinctive morphology from DGR and other reported electrochemical synthesized GR[29,30] will support the sensitivity of an electrode as an electrochemical sensor.

Distinctively, a relatively smooth and flat surface was obtained after the modification of ZnO nanoparticles (Fig. 1D). As seen from the cross-section views, ZnO nanoparticles were well-confined in the EGR film with nano sizes. It could be speculated that the metal oxide nanoparticles crystallized and padded along the corrugated structure of the EGR. As a result, ZnO particles are closely protected by the corrugated EGR film which offered high mechanical durability and large surface areas to prohibit the nanoparticles from aggregation, sintering, and dissolution. It is also expected that the displayed cooperation of ZnO and EGR will boost the stability and sensitivity of GCE in electrochemical sensing.

3.1.2 X-ray photoelectron spectroscopy. The chemical composition changes during the modification were further monitored by XPS, as shown in Fig. 2. The C 1s in DGR, EGR and EGR–ZnO was clearly detected at around 284.6 eV to ensure the existence of GR. Due to the chemical reduction method of GR, some residual oxygen groups still exist in its sheets, which contributes to the O 1s peak at 531 eV in DGR. The C/O intensity ratio decreased from 7.1 in DGR to 6.0 in EGR, demonstrating the oxidation of GR during the electrodeposition process. The Zn 2p XPS spectra in the figure shows two major peaks with binding energy values at 1022 and 1045 eV, corresponding to the Zn $2p_{3/2}$ and Zn $2p_{1/2}$ spin-orbit peaks, respectively (Fig. 2B).

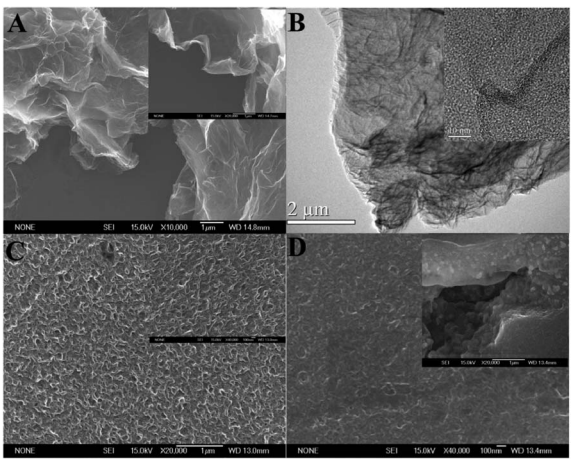

Fig. 1 (A) SEM of DGR. Inset is the amplifying photograph. (B) TEM and HRTEM (inset) images of DGR. (C) SEM image of EGR with a magnification inset. (D) SEM of ZnO–EGR nanocomposite. The inset is the transection image of the nanocomposite.

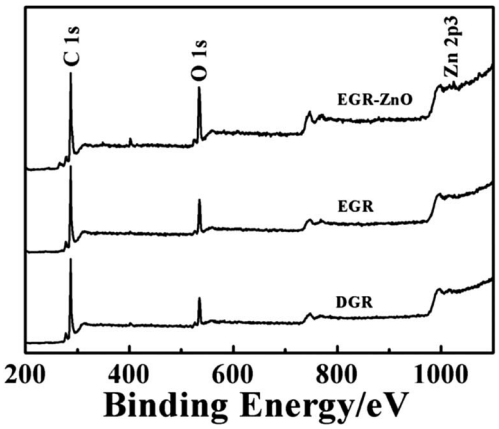

Fig. 2 XPS survey spectra of DGR, EGR and EGR–ZnO.

These evidences, accompanied by the O 1s peak at 531 eV, indicate the presence of ZnO nanoparticles.

3.1.3 Raman spectroscopy. Raman spectroscopy is a powerful nondestructive tool to distinguish ordered and disordered crystal structures of carbon. The G-band, which originates from the first-order scattering from the doubly degenerate E_{2g} phonon modes of graphite in the Brillouin zone center, is characteristic of all sp^2-hybridized carbon networks, while the prominent D peak is a breathing mode of *k*-point phonons of A_{1g} symmetry, assigned to structural imperfections created by the attachment of oxygenated groups on the carbon basal plane.[31–33] Thus, the intensity ratio of the D and G bands (I_D/I_G) offers not only clues to the oxidation degree and the size of sp^2 ring clusters in a network of sp^3 and sp^2 bonded carbon,[34] but also the degree of defects and disorder of the graphitized structures.[35,36] Fig. 3 illustrates the Raman spectra of the DGR, EGR and EGR–ZnO nanocomposite with a distinguished increase of D/G intensity ratio. Specifically, the intensity ratio increased from 0.765 of DGR to 1.016 of EGR, and then further increased to 1.296 after the successful modification of ZnO onto EGR. The two prominent peaks of the D and G bands also

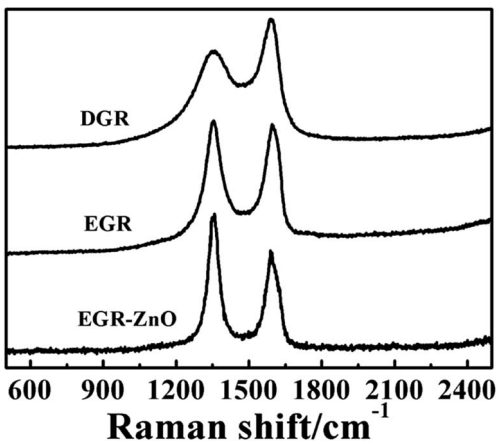

Fig. 3 Raman spectra of the DGR, EGR and EGR–ZnO nanocomposite. All data were acquired at 514.5 nm excitation.

shifted from 1345.6 and 1592.9 cm^{-1} of DGR to 1352.1 and 1601.1 cm^{-1} of EGR, then to 1355.8 and 1595.5 cm^{-1} of the nanocomposite.

In accordance with SEM and XPS results, the intensity ratio increase accompanied with wave shifts indicated that the EGR exhibited a different status from DGR, with an increasing degree of defects and disorder of the graphitized structures owing to the electrodeposition. In addition, a decrease in the average size of the sp^2 domains was speculated to occur upon electrodeposition, which was caused by the creation of numerous new graphitic domains in EGR that are smaller in size than the ones presented in DGR.[34] In addition, the changes also verified that ZnO nanoparticles preferably grew and formed strong coupling interactions with EGR, with its characteristic peak at 438 cm^{-1} (Fig. S2, ESI†).

3.2 Electrochemical study of EGR and DGR

In order to probe the electrochemical performance of EGR and DGR, electrochemical impedance spectroscopy (EIS) and CV in 5 mM $K_3Fe(CN)_6$–$K_4Fe(CN)_6$ was further performed. EIS is a powerful tool for studying the interface properties of the modified electrode and can provide information on the impedance changes of the interface of the electrode surface–electrolyte solution. The Nyquist plots of the EIS consist of a semicircular portion and a linear portion, which corresponds to the electron transfer limited process and the diffusion limited process, respectively.

Explicit illustrations of impedance change with the sequential modification of DGR, EGR and EGR–ZnO on to GCE are shown in Fig. 4A. Evidently, DGR markedly reduced the impedance of GCE while EGR exhibited a considerably large semi-circle, indicating relatively large impedance. Correspondingly, the CV currents in Fig. 4B suggested higher ETR on DGR/GCE than EGR/GCE. With respect to ΔE_p, a major indicator of electrode reversibility, changed from 92 Ω with bare GCE to 98 Ω with DGR/GCE, and further increased to 111 Ω for EGR/GCE. All this evidence, echoing the results of the XPS and Raman spectra, accordingly attested that electrodeposition had given rise to remarkable structure defects on EGR concomitant of some loss in electrical conductivity. However, ZnO/EGR/GCE presented a remarkably diminished impedance, which was similar to that of bare GCE, and a slightly improved CV in $K_3Fe(CN)_6/K_4Fe(CN)_6$ with the narrowest potential separation between the anodic and cathodic peaks (ΔE_p of 83 Ω). This evidence suggested an enhanced conductivity as well as reversibility of ZnO/EGR/GCE when compared to a bare GCE.

To further explore the sensing performance for AC, square wave voltammetry (SWV), a powerful electrochemical technique that can be applied in both electrochemical kinetics and analytical measurements, was carried out in 10 mL PBS (pH 6) containing 10 μM AC for DGR/GCE, ZnO/DGR/GCE and ZnO/EGR/GCE(Fig. 4C). It is evident that the current of AC increased 4-fold at ZnO/DGR/GCE, while the current response dramatically peaked at ZnO/EGR/GCE with a value 16-times that on bare GCE. It turned out that ZnO/EGR/GCE possessed a more desirable sensitivity to AC than ZnO/DGR/GCE.

To sum up, the apparently diminished impedance at ZnO/EGR/GCE can be mainly attributed to the electroactive properties of ZnO nanoparticles to ferricyanide.[37] With respect to AC, the electrocatalytic ability of EGR and ZnO to AC cooperatively contribute towards the sensitive response. Moreover, the enhanced reversibility at ZnO/EGR/GCE demonstrates that the unique structure and synergistic effect of the EGR–ZnO hybrid *via* the proposed preparation also allow efficient electron transfer and better mass transport of the reactants to the electroactive sites on the electrode surface.[38]

Owing to the oxidation of EGR, the positively charged Zn^{2+} ions will be attracted towards the negatively charged EGR *via* electrostatic driving forces, and thus further grew along the corrugated film. The formation of ZnO nanoparticles can be possibly explained by the following mechanistic pathways:[39,40]

$$Zn^{2+} + NO^{3-} + 2e^- \rightarrow ZnO + NO^{2-} \quad (1)$$

$$Zn^{2+} + 1/2O_2 + 2e^- \rightarrow ZnO \quad (2)$$

3.3 Electrochemical behavior of the proposed sensor

3.3.1 CVs of modified electrodes to AC. The EGR–ZnO nanocomposite modified GCE was firstly employed to determine AC alone. Fig. 5A reveals the CVs of the bare GCE (curve a), EGR/GCE (curve b), ZnO/GCE (curve c) and ZnO/EGR/GCE (curve d) in 0.1 M PBS (pH 6.0) containing 10 μM AC at the scan rate of 100 mV s^{-1}. It was observed that EGR/GCE and ZnO/GCE respectively improved the oxidation current 3.4 and 3.2 times of that on GCE, while ZnO/EGR/GCE extraordinarily improved the

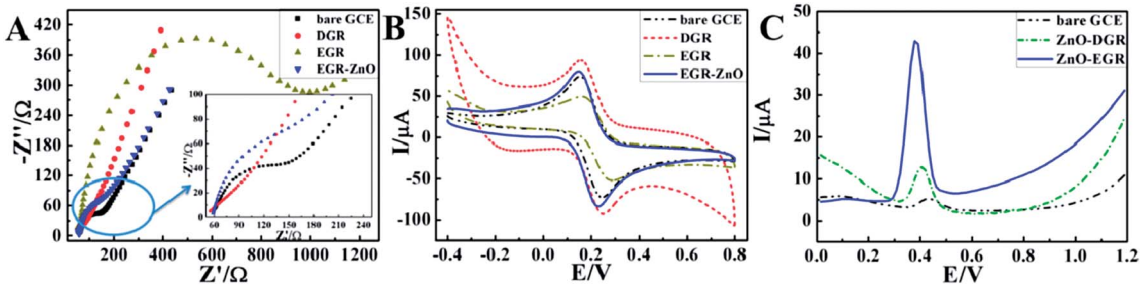

Fig. 4 Nyquist plot of EIS (A) and CVs (B) for bare GCE, DGR/GCE, EGR/GCE, and ZnO/EGR/GCE in 5 mM $K_3Fe(CN)_6$–$K_4Fe(CN)_6$; (C) SWVs of 10 μM AC on bare GCE, ZnO/DGR/GCE and ZnO/EGR/GCE in 0.1 M PBS (pH 6).

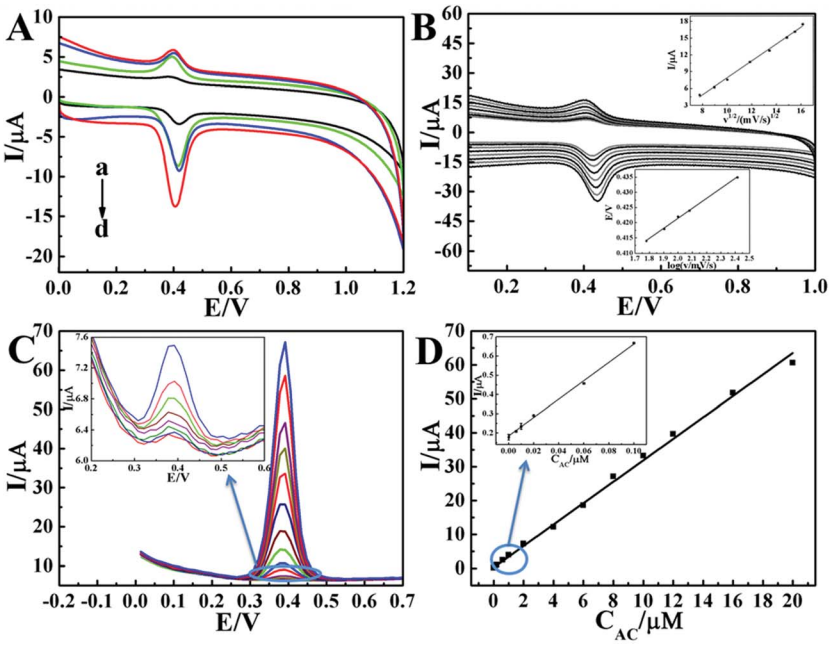

Fig. 5 (A) CVs of bare GCE (a), ZnO/GCE (b), EGR/GCE (c) and ZnO/EGR/GCE (d) in 0.1 M PBS (pH 6.0) containing 10 μM AC at the scan rate of 100 mV s^{-1}. (B) CVs of ZnO/EGR/GCE in 0.1 M PBS (pH 6) with 10 μM AC at scan rate of 60 to 260 mV s^{-1}. Insets are linear relationships of $v^{1/2}$ *vs.* *I* and log *v* *vs.* E_p. (C) SWVs of ZnO/EGR/GCE at concentrations of AC ranging from 10^{-4}–20 μM in 0.1 M PBS (pH 6.0). Inset is the SWVs at low concentrations. (D) Calibration curve for the determination of AC.

current value by 5-fold. Moreover, the ZnO/EGR/GCE also negatively shifted the oxidation potential by 14 mV more than that on bare GCE. Corresponding to the results in Fig. 4C, it is undeniable that the oxidation activity to AC is effectively boosted at ZnO/EGR/GCE, benefiting from the catalytic properties and a high surface-to-volume ratio of the nanocomposite as well as the synergistic effect of ZnO and EGR as a whole.

3.3.2 The optimization of buffer solution pH and modification time. SWVs in 0.1 M PBS with its pH ranging from 2 to 8 were applied to evaluate the pH impact on the current signals (Fig. S1A, ESI†). From the figure, the oxidation current of AC peaked at pH 6, and then decreased even with the continuous increase of pH value. Ultimately, pH 6 was chosen as the optimal condition of the supporting electrolyte. In addition, the linear relationship of E_p *vs.* pH implied equal protons and electrons were involved in the oxidation of AC.

The accumulation of the ZnO nanoparticles on the electrode also plays an important role in terms of sensor performance. Fig. S1B, ESI† describes the relationship between the current value of AC and the modification time. It was obvious that the AC oxidation current on ZnO/EGR/GCE reached the highest point when the number of ZnO modification cycles was 25. Accordingly, 25 cycles was determined to be the optimal modification condition for ZnO nanoparticles.

3.3.3 The effect of scan rate. CV experiments were carried out to investigate the influence of scan rate at ZnO/EGR/GCE in 0.1 M PBS (pH 6) containing 10 μM AC (Fig. 5B). An evident linear relationship between the square root of the scan rate ($v^{1/2}$) and the oxidation peak current (I_p) in the range of 60–260 mV s^{-1} was obtained. The linear equation was described as: $I_p = -7.218 + 1.512v^{1/2}$ ($R = 0.998$), validating the oxidation of AC as a diffusion-controlled process. Meanwhile, there was a positive shift of potential with the increase of scan rate, and the logarithm of scan rate (log *v*) *vs.* the anodic peak potential (E_p) appeared to have a proportional relationship. The equation for log *v* and E_p was: $E_p = 0.3555 + 0.03295 \log v$ ($R = 0.999$). An equation for the irreversible process is described as following:

$$E_p = 2.303RT/2(1 - \alpha)nF \log v + K \quad (3)$$

where α is the electron transfer coefficient, *n* is the number of electrons involved in the rate-controlling step, *R*, *T* and *F* are the gas constant, temperature and Faraday constant, respectively.

On the basis of the slope being equal to $2.303RT/2(1 - \alpha)nF$, the value of $(1 - \alpha)n$ is calculated to be 0.897. The electron transfer coefficient α is assumed as 0.5 for an irreversible electrode process, then the number of transferred electrons is *ca.* 2, which is consistent with the reported literature.[41] Following is the inferred mechanism of AC oxidation (Scheme 1).

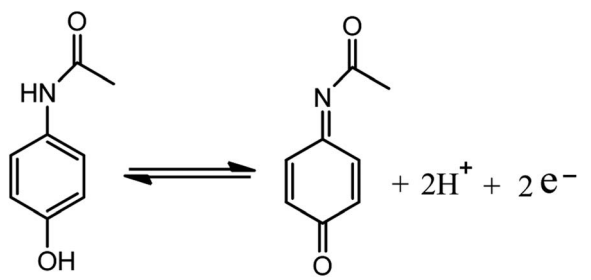

Scheme 1 The mechanism of AC oxidation.

3.3.4 Determination of AC on ZnO/EGR/GCE. The determination of AC with different concentrations under the optimized experimental conditions on ZnO/EGR/GCE was shown in Fig. 5C and D. There is a distinct linear relationship between the peak currents of AC and its concentration in the range of 0.1 nM to 20 μM. The regression equation was described as: I_p (μA) = 0.2458 + 3.163 C (μM) (R = 0.999) with a sensitivity and detection limit of 44 774.24 μA mM^{-1} cm^2 and 3.3 × 10^{-5} μM, respectively.

Compared with previous works, ZnO/EGR/GCE possessed a remarkable sensitivity and a far lower detection limit of AC determination. Table 1 illustrates the reported works on detection of AC over recent years.

3.4 Simultaneous determination of AC and PCT

3.4.1 Effect of electrolyte pH on simultaneous determination. The effect of electrolyte pH on the simultaneous detection of AC and PCT on ZnO/EGR/GCE was studied and shown in Fig. 6A. The oxidation current of AC reached its peak at pH 6 while PCT peaked at pH 3. The peak separation between AC and PCT, a vital reference factor for simultaneous determination, increased until the pH value reached 8 and after then decreased. Taking the potential separation as well as the current changes into account, pH 6 was assumed to be the most suitable pH for simultaneous determination.

3.4.2 Simultaneous determination of AC and PCT on ZnO/EGR/GCE. The linear detection of AC and PCT on ZnO/EGR/GCE is implemented by SWV in 0.1 M PBS (pH 6.0). It is revealed that two separate and distinct peaks of AC and PCT were observed in Fig. 6B. The calibration curves of AC and PCT were shown in Fig. 6C with the linear relationship from 0.02 to 10 μM for AC and 0.06 to 10 μM for PCT. The linear equations for AC and PCT were described as following: I_{AC} (μA) = 0.5718 + 3.836C (μM) (R = 0.998) and I_{PCT} (μA) = 0.05866 + 1.508C (μM) (R = 0.999). The sensitivities were calculated to be 54 295.82 μA mM^{-1} cm^2 for AC and 21 344.66 μA mM^{-1} cm^2 for PCT, respectively. These results synergistically proved the feasibility of simultaneous determination and distinguished electrochemical sensing performance of ZnO/EGR/GCE to AC and PCT.

Table 1 Comparisons of the proposed ZnO/EGR/GCE with previous reported electrochemical methods for AC determination[a]

Modified electrodes	Technique	Linear working range (μM)	Detection limit (μM)	Ref.
P4VP/MWCNT/GCE	DPV	0.02–450	0.00169	41
C–Ni/GCE	DPV	2.0–230	0.6	42
CNT/SPCE	CV	2.5–2000	0.1	43
CNT/TCPE	DPV	0.1–100	0.05	44
GR/GCE	SWV	2–230	0.6	45
Nafion/TiO_2–GR/GCE	DPV	1–100	0.21	46
ETPGE	ATSDPV	0.05–2.5	2.5 × 10^{-3}	47
D50wx2/GNP/GCPE	AdSSWV	0.0334–42	4.7 × 10^{-3}	48
nPt–MWCNTPE	DPV	0.5–100	0.17	49
SWCNT–GNS/GCE	DPV	0.05–64.5	0.038	50
AuNP–PGA/SWCNE	DPV	8.3–145.6	1.18	51
Fe_3O_4/PDDA/GR/GCE	DPV	0.1–100	0.037	52
LNT–CFO/GCE	I-T	0.5–901	0.19	53
ZnO/EGR/GCE	SWV	10^{-4}–20	3.3 × 10^{-5}	This work

[a] P4VP/MWCNT/GCE: poly(4-vinylpyridine)/multiwalled carbon nanotubes modified glassy carbon electrode. CNT/SPCE: carbon nanotubes modified screen-printed carbon electrode. CNT/TCPE: multi-walled carbon nanotube/thionine modified carbon paste electrode. ETPGE: the electrochemically treated pencil graphite electrode. D50wx2/GNP/GCPE: a cation exchanger resin, Dowex 50wx2 and gold nanoparticles modified glassy carbon paste electrode. nPt–MWCNTPE: multi-walled carbon nanotube and Pt-nanoparticles modified carbon paste electrode. SWCNT–GNS/GCE: single-walled carbon nanotube–graphene nanosheet hybrid film modified electrode. AuNP–PGA/SWCNE: co-deposit in glutamic acid and gold nanoparticles on a single-walled carbon nanotube film electrode. Fe_3O_4/PDDA/GR/GCE: Fe_3O_4 nanoparticles-coated poly(diallyldimethylammonium chloride)-functionalized graphene nanocomposite film. LNT–CFO/GCE: $LaNi_{0.5}$–$Ti_{0.5}O_3$/$CoFe_2O_4$ nanoparticle-modified electrode.

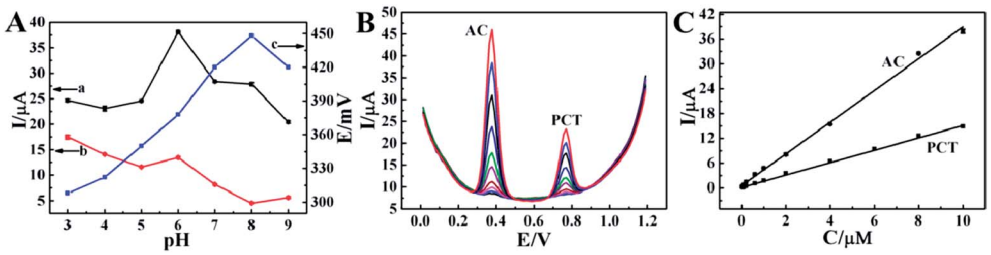

Fig. 6 (A) Effect of pH on the peak currents of AC (a) and PCT (b) and the potential separation between AC and PCT peaks (c) on ZnO/EGR/GCE in 0.1 M PBS with pH ranging from 3.0 to 9.0. (B) SWVs of ZnO/EGR/GCE at different concentrations of AC and PCT in 0.1 M PBS (pH 6.0). (C) Calibration curves for the determination of AC (0.02–10 μM) and PCT (0.06–10 μM).

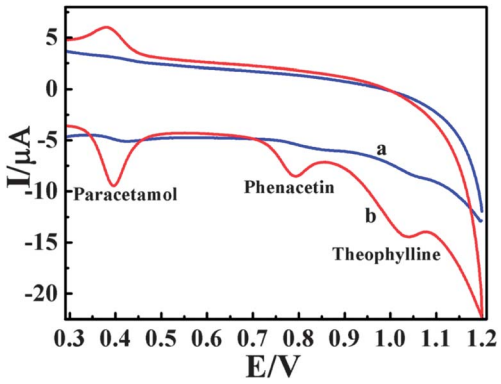

Fig. 7 CVs of bare GCE (a) and ZnO/EGR/GCE (b) in 0.1 M PBS (pH 6) containing 10 μM AC, 10 μM PCT and 20 μM theophylline.

Table 2 Determination of AC and PCT in pharmaceutical products and human serum samples ($n = 3$)

	Added (μM)		Detected (μM)		Recovery (%)	
No.	AC	PCT	AC	PCT	AC	PCT
Tablets	2.481	0.837	2.494	0.850	101.5	100.5
	4.962	3.348	4.937	3.329	99.5	99.4
	8.270	5.022	8.233	5.026	99.5	100.0
Human serum	1.654	0.837	1.646	0.798	99.5	95.4
	2.481	4.185	2.285	4.109	92.1	98.2
	8.270	5.022	8.522	4.946	103.0	98.5

3.5 Reproducibility and stability studies

The reproducibility of ZnO/EGR/GCE was examined by using the same electrode for 6 repetitive measurements of 10 μM AC under the optimum conditions. The relative standard deviation was calculated to be 0.54% for AC and 2.12% for PCT, which indicated good reproducibility. Furthermore, ZnO/EGR/GCE was proved to be very stable towards simultaneous determination of AC and PCT with the oxidation currents of AC and PCT only losing 8.3% and 4.1%, respectively, after preserving the sensor in the refrigerator for 10 days, reflecting the excellent stability of the proposed sensor.

3.6 Interference studies

The selectivity and anti-interference properties of the proposed sensor were carried out by simultaneously determining the target molecule and interferents. The tolerance limit was taken as the maximum concentration of other foreign substances that caused a relative error of ±5% in the determination. The result of interference is shown in Table S1, ESI.† Experiment results illustrated that 5-fold of phenylalanine, alanine and leucine, 10-fold sucrose, maltose, sucrose and Al^{3+} and Cu^{2+}, and 20-fold glucose and NaCl together with 40-fold citric acid hardly caused interference.

Theophylline is a kind of methylxanthine drug often used in therapy for respiratory diseases, such as chronic obstructive pulmonary disease (COPD) and asthma. There is a great possibility of theophylline interfering in the determination of AC and PCT since it may coexist with them. Therefore, to further validate the anti-interference of the proposed sensor, determination of AC and PCT coexisting with theophylline was illustrated in Fig. 7. It exhibited well-defined and significantly improved CV responses at ZnO/EGR/GCE in 0.1 M PBS (pH 6.0) compared with bare GCE. This not only further affirmed that the sensor possessed excellent selectivity and anti-interference ability for the detection of AC and PCT, but proved its stably catalytic properties.

3.7 Analysis of real samples

To further verify the practical performance of the proposed sensor, ZnO/EGR/GCE was applied to determine AC and PCT in their tablet samples as well as in a human serum environment. Before determination, the prepared stock solution was diluted from 1.0 to 10.0 mL, then 10 mL of the diluted samples were injected into 10 mL of the 0.1 M PBS (pH 6.0). The results were summarized and listed in Table 2. Satisfactory recovery for real samples demonstrated that the proposed sensor held great promise for reliable and sensitive application in the field of pharmaceutical analysis.

4 Conclusion

A facile and novel EGR–ZnO composite has been synthesized *via* potentiostatic deposition and cyclic voltammetry techniques. The EGR was confirmed to be partially oxidized and formed a unique 3D structure with ZnO nanoparticles, mutually facilitating the electrocatalytic activity, electron transfer and mass transport. As a result, an ultrasensitive electrochemical sensor for AC and PCT based on the EGR–ZnO nanocomposite was fabricated with desirable detection results in real samples. In conclusion, our proposed strategy of EGR–transition metal oxide here can be broadened as an effective approach for EGR-based inorganic composites for bioanalysis, biosensing and even other related fields like supercapacitor sand lithium ion batteries.

Acknowledgements

This work is supported by the National Natural Science Foundation of China (no. 21271127, 61171033), the NanoFoundation of Science and Techniques Commission of Shanghai Municipality (no. 12nm0504200, 12dz1909403), Leading Academic Discipline Project of Shanghai Municipal Education Commission (J50102). We acknowledge the Instrumental Analysis & Research Centre, Shanghai University. The authors would like to acknowledge Dr Yuliang Chu for the FESEM.

References

1 J. S. Zhou, L. L. Ma, H. H. Song, B. Wu and X. H. Chen, *Electrochem. Commun.*, 2011, **13**, 1357–1360.
2 M. Sathish, T. Tomai and I. Honma, *J. Power Sources*, 2012, **217**, 85–91.

3 Y. X. Xu, X. Q. Huang, Z. Y. Lin, X. Zhong, Y. Huang and X. F. Duan, *Nano Res.*, 2013, **6**, 65–76.
4 H. J. Huang and X. Wang, *Nanoscale*, 2011, **3**, 3185–3191.
5 J. W. Zhu, S. Chen, H. Zhou and X. Wang, *Nano Res.*, 2012, **5**, 11–19.
6 M. X. Li, J. E. Zhu, L. L. Zhang, X. Chen, H. M. Zhang, F. Z. Zhang, S. L. Xu and D. G. Evans, *Nanoscale*, 2011, **3**, 4240–4246.
7 Q. W. Chen, L. Y. Zhang and G. Chen, *Anal. Chem.*, 2012, **84**, 171–178.
8 H. D. Jang, S. K. Kim, H. Chang, K. M. Roh, J. W. Choi and J. X. Huang, *Biosens. Bioelectron.*, 2012, **38**, 184–188.
9 D. X. Ye, L. Q. Luo, Y. P. Ding, B. D. Liu and X. Liu, *Analyst*, 2012, **137**, 2840–2845.
10 L. Jiang, S. Q. Gu, Y. P. Ding, D. X. Ye, Z. Zhang and F. F. Zhang, *Colloids Surf., B*, 2013, **107**, 146–151.
11 Y. Hernandez, V. Nicolosi, M. Lotya, F. Blighe, Z. Y. Sun, S. De, I. T. McGovern, B. Holland, M. Byrne, Y. Gunko, *et al.*, *Nat. Nanotechnol.*, 2008, **3**, 563–568.
12 R. Zacharia, H. Ulbricht and T. Hertel, *Phys. Rev. B: Condens. Matter Mater. Phys.*, 2004, **69**, 155406–155407.
13 M. D. Stoller, S. J. Park, Y. W. Zhu, J. H. An and R. S. Ruoff, *Nano Lett.*, 2008, **8**, 3498–3502.
14 D. S. Yu and L. M. Dai, *J. Phys. Chem. Lett.*, 2010, **1**, 467–470.
15 Y. Wang, Z. Q. Shi, Y. Huang, Y. F. Ma, C. Y. Wang, M. M. Chen and Y. S. Chen, *J. Phys. Chem. C*, 2009, **113**, 13103–13107.
16 H. L. Guo, X. F. Wang, Q. Y. Qian, F. B. Wang and X. H. Xia, *ACS Nano*, 2009, **3**, 2653–2659.
17 C. Malitesta, I. Losito and P. G. Zambonin, *Anal. Chem.*, 1999, **71**, 1366–1370.
18 T. C. Tsai, H. Z. Han, C. C. Cheng, L. C. Chen, H. C. Chang and J. J. J. Chen, *Sens. Actuators, B*, 2012, **171–172**, 93–101.
19 H. D. Li, H. M. Guan, H. Dai, Y. J. Tong, X. Zhao, W. J. Qi, S. Majeed and G. B. Xu, *Talanta*, 2012, **99**, 811–815.
20 L. Feng, Y. J. Liu, Y. Y. Tan and J. M. Hu, *Biosens. Bioelectron.*, 2004, **19**, 1513–1519.
21 C. L. Choong and W. I. Milne, *Biosens.Bioelectron.*, 2010, **25**, 2384–2388.
22 A. Menaker, V. Syritski, J. Reut, A. Öpik1, V. Horváth and R. E. Gyurcsányi, *Adv. Mater.*, 2009, **21**, 2271–2275.
23 V. Syritskia, J. Reuta, A. Menakera, R. E. Gyurcsányib and A. Öpik, *Electrochim. Acta*, 2008, **53**, 2729–2736.
24 E. Mazzottaa, C. Malitestaa, M. Díaz-Álvarezb and A. Martin-Estebanb, *Thin Solid Films*, 2012, **520**, 1938–1943.
25 A. Österholma, T. Lindforsa, J. Kauppilab, P. Damlinb and C. Kvarnströmb, *Electrochim. Acta*, 2012, **83**, 463–470.
26 Y. Lattach, P. Archirel and S. Remita, *J. Phys. Chem. B*, 2012, **116**, 1467–1481.
27 X. W. Kan, H. Zhou, C. Li, A. H. Zhu, Z. L. Xing and Z. Zhao, *Electrochim. Acta*, 2012, **63**, 69–75.
28 Y. H. Zhu, Z. L. Zhang, W. Zhao and D. W. Pang, *Sens. Actuators, B*, 2006, **119**, 308–314.
29 H. T. Zhang, X. Zhang, D. C. Zhang, X. Z. Sun, H. Lin, C. H. Wang and Y. W. Ma, *J. Phys. Chem. B*, 2013, **117**, 1616–1627.
30 J. Yang, X. B. Yan, J. T. Chen, H. B. Ma, D. F. Sun and Q. J. Xue, *RSC Adv.*, 2012, **2**, 9665–9670.
31 D. Yang, A. Velamakanni, G. Bozoklu, S. Park, M. Stoller, R. D. Piner, S. Stankovich, I. Jung, D. A. Field and C. A. Ventrice, *Carbon*, 2009, **47**, 145–152.
32 M. A. Pimenta, G. Dresselhaus, M. S. Dresselhaus, L. G. Cancado, A. Jorio and R. Saito, *Phys. Chem. Chem. Phys.*, 2007, **9**, 1276–1291.
33 M. S. Dresselhaus, G. Dresselhaus and M. Hoffmann, *Philos. Trans. R. Soc., A*, 2008, **366**, 231–236.
34 C. Mattevi, G. Eda, S. Agnoli, S. Miller, K. A. Mkhoyan, O. Celik, D. Mastrogiovanni, G. Granozzi, E. Garfunkel and M. Chhowalla, *Adv. Funct. Mater.*, 2009, **19**, 2577–2583.
35 D. Graf, F. Molitor, K. Ensslin, C. Stampfer, A. Jungen, C. Hierold and L. Wirtz, *Nano Lett.*, 2007, **7**, 238–242.
36 F. Tuinstra and J. L. Koenig, *J. Chem. Phys.*, 1970, **53**, 1126–1130.
37 X. C. Dong, Y. F. Cao, J. Wang, M. B. Chan-Park, L. H. Wang, W. Huang and P. Chen, *RSC Adv.*, 2012, **2**, 4364–4369.
38 D. Chen, H. B. Feng and J. H. Li, *Chem. Rev.*, 2012, **112**, 6027–6053.
39 M. Izaki and T. Omi, *Appl. Phys. Lett.*, 1996, **68**, 2439–2440.
40 M. Izaki and T. Omi, *J. Electrochem. Soc.*, 1996, **143**, L53–L55.
41 H. Ghadimi, R. M. A. Tehrani, A. S. Mohamed Ali, N. Mohamed and S. Ab Ghani, *Anal. Chim. Acta*, 2013, **765**, 70–76.
42 S. F. Wang, F. Xie and R. F. Hu, *Sens. Actuators, B*, 2007, **123**, 495–500.
43 P. Fanjul-Bolado, P. J. Lamas-Ardisana, D. Hernández-Santos and A. Costa-García, *Anal. Chim. Acta*, 2009, **638**, 133–138.
44 S. Shahrokhian and E. Asadian, *Electrochim. Acta*, 2010, **55**, 666–672.
45 X. H. Kang, J. Wang, H. Wu, J. Liu, I. A. Aksay and Y. H. Lin, *Talanta*, 2010, **81**, 754–759.
46 Y. Fan, J. H. Liu, H. T. Lu and Q. Zhang, *Colloids Surf., B*, 2011, **85**, 289–292.
47 A. Özcan and Y. Sahin, *Anal. Chim. Acta*, 2011, **685**, 9–14.
48 B. J. Sanghavi and A. K. Srivastava, *Anal. Chim. Acta*, 2011, **706**, 246–254.
49 J. B. Raoof, M. Baghayeri and R. Ojani, *Colloids Surf., B*, 2012, **95**, 121–128.
50 X. Chen, J. Zhu, Q. Xi and W. S. Yang, *Sens. Actuators, B*, 2012, **161**, 648–654.
51 M. P. N. Bui, C. A. Li, K. N. Han, X. H. Pham and G. H. Seong, *Sens. Actuators, B*, 2012, **174**, 318–324.
52 D. B. Lu, Y. Zhang, L. Wang, S. X. Lin, C. M. Wang and X. F. Chen, *Talanta*, 2012, **88**, 181–186.
53 D. X. Ye, Y. H. Xu, L. Q. Luo, Y. P. Ding, Y. L. Wang and X. J. Liu, *J. Solid State Electrochem.*, 2012, **16**, 1635–1642.